ORIGINAL

Dimosthenis Floros · Andreas Jobst [ORCID] **· Andreas Kergaßner ·
Marion Merklein · Paul Steinmann**

Towards an holistic account on residual stresses in full-forward extruded rods

Experiment, modeling and simulation of forming and operation phases

Abstract An holistic view is attempted towards prediction of the effect of residual stresses induced by full-forward extrusion on fatigue life of workpieces during operation. To study the effect of constitutive model on the accuracy of forming simulations, a combined nonlinear isotropic/kinematic hardening model as well as the isotropic hardening part of the same model are calibrated based on five compression-tension-compression uniaxial stress experiments. A full-forward extrusion finite element model is developed adapting both the aforementioned hardening plasticity models and the predicted residual stress states at the surface of the workpiece are compared against that of a corresponding forming experiment. Results show residual stress predictions of remarkable accuracy by the FE-models with the isotropic hardening model. The effect of residual stresses on fatigue life of the workpiece is qualitatively studied by uncoupled multiscale simulations featuring gradient crystal plasticity at the microscale. While the effective (homogenized) macroscale response indicates elastic response during a macroscopically cyclic loading, plasticity accompanying reduction of residual stresses is still present at the microscale within, e.g. grain boundaries.

1 Introduction

Forward rod extrusion is a well-established method for manufacturing metal components such as screws, bolts and axles in large series. Forming at room temperature allows a material and energy-efficient production of high quality parts. Due to work hardening, a high material strength is achievable. However, inhomogeneous plastic flow during forming causes residual stresses to remain within the formed parts. Depending on their magnitude and stability [1], they may influence the parts operating behaviour [2]. Tensile residual stresses, for example, are superimposing load stresses, resulting in reduced fatigue resistance [3]. Compressive residual stresses on the other hand counteract crack initiation and growth [4].

If these stresses are taken into account already during the virtual product design, it is possible to shorten the production cycle through the elimination of subsequent heat treatment steps. For an accurate numerical computation of the forming process and the resulting part properties, a detailed modelling of the material behaviour is necessary. For simple forming processes, an isotropic material model may be sufficient. However, as soon as a load reversal occurs during the process, the Bauschinger effect leads to a reduction of the yield

D. Floros · A. Kergaßner · P. Steinmann
Institute of Applied Mechanics, Friedrich-Alexander Universität Erlangen-Nürnberg, Egerlandstr. 5, 91058 Erlangen, Germany
E-mail: dimosthenis.floros@fau.de

A. Jobst (✉) · M. Merklein
Institute of Manufacturing Technology, Friedrich-Alexander Universität Erlangen-Nürnberg, Egerlandstr. 13, 91058 Erlangen, Germany
E-mail: andreas.aj.jobst@fau.de

stress [5]. Therefore, a combined isotropic-kinematic hardening model is required for an accurate numerical computation of forming processes.

The isotropic hardening behaviour is determined in uniaxial tests with tensile or compressive load. These tests have the advantage of being comparatively simple to conduct and applicable to both sheet metal and bars. Compressive tests are limited by buckling and bulging of the specimens [6], while in tensile tests, necking and breaking of the material are critical. For the determination of combined isotropic-kinematic hardening parameters, tests are carried out, where the loading direction is changing. When analysing cyclic plasticity, specific phenomena such as the Bauschinger effect, recovery and ratchetting are occurring [7]. Experimental methods are mainly focused on the testing of sheet metal [8], where combined hardening parameters are necessary for springback calculation [9]. For the reproduction of specific stress states, different loading types are considered, such as bending [10], shearing [11] and uniaxial tension and compression [12]. The latter is particularly interesting for the testing of bar-shaped material. Due to buckling of the specimen, tests with large strains are difficult to perform on sheet metal.

From a numerical modeling point of view, computation of the residual stress state comprises typically the last (postprocessing) step in Finite Element (FE) simulations of cold metal forming processes such as forward rod extrusion. Residual stresses, though, are generated during the whole forming process due to inhomogeneous plastic deformation [13]. Thereby, the quality of the predicted residual stress state depends at large on the validity of the numerical model used to model the whole forming process. Modeling of full-forward extrusion for example involves large inelastic strains and (normal and frictional) contact between different modeling parts (e.g. workpiece, punching tool, die etc.). These are some of the influencing factors that may affect accuracy of the numerical model [14]. To enhance validity of numerical model in the finite strain regime, emphasis is laid on, e.g. appropriateness of the spatial discretization (FE-mesh) with respect to forming procedure (viz. process adopted mesh [15] and remeshing) and, moreover, ability of the employed constitutive model to accurately describe the Bauschinger as well as transient effects that are typically encountered in forming.

With regards to the latter, modeling of kinematic hardening at finite strains may have a significant effect on predicted residual stresses after forming, especially in cases of multistage forming [14]. In the absence of a calibrated constitutive model for X6Cr17 (1.4016) under cyclic loading, calibration of a Chaboche [16] combined nonlinear isotropic/kinematic hardening model is performed here. As input to the calibration, five uniaxial stress experiments were conducted, each featuring a compression-tension-compression cycle at increasing strain amplitudes.

Metal forming process parameters (e.g. shoulder angle and diameter change prior and after forming, sequence of execution) have an effect on the residual stress state after forming [17], which, in turn, has an effect on fatigue life during operation [18,19]. Thereby, robust modeling of both the forming and the operation phases is a prerequisite for a correct numerical evaluation of the effect of different forming process parameters on fatigue life during operation. In this regard, FE-modeling of a full-forward extrusion experiment with ejection of the workpiece is performed, adopting combined isotropic/kinematic as well as pure isotropic hardening models for the workpiece. Predicted residual stresses at the surface of the formed workpiece are compared against the experimentally measured. In addition, as a precursor to future work on coupled multiscale modeling of the operation phase, the effect of residual stresses on the fatigue life of a formed component is qualitatively studied via uncoupled multiscale modeling featuring a gradient crystal plasticity model [20] at the microscale.

The paper is organized as follows: Uniaxial stress experiments with the ferritic stainless steel X6Cr17 (1.4016) are conducted and corresponding material response at finite strains is modeled in Sect. 2. Residual stresses induced by full-forward rod extrusion with the aforementioned steel are experimentally and numerically investigated in Sect. 3. The effect of residual stresses on fatigue life of an extruded specimen is qualitatively studied in Sect. 4 via uncoupled multiscale FE-simulations. Performance of the employed experimental and numerical methods for measurement and prediction of residual stresses are discussed in Sect. 5 and conclusions are outlined in Sect. 6.

2 Material characterization

2.1 Experiment – cyclic plastification tests

For testing bar-shaped material, different challenges are arising. In order to prevent measuring errors caused by sliding of the specimens in clamping tools, a form-locking force transmission is necessary. Exact positioning of
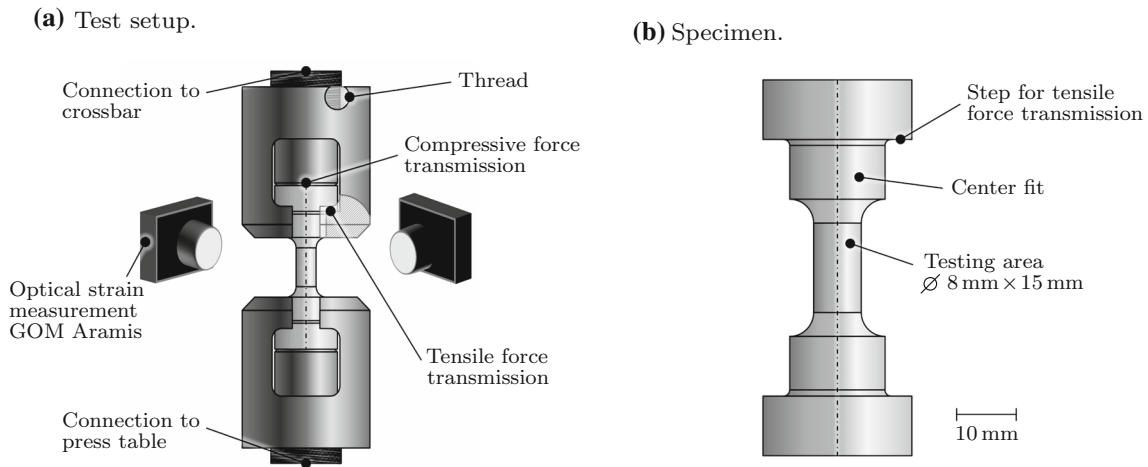
(a) Test setup.

(b) Specimen.

Fig. 1 Cyclic plastification tests

the samples in the holders is necessary to ensure a central transmission of force. In order to meet the challenges regarding cyclic plastification tests, the setup and the specimen geometry shown in Fig. 1 have been developed. A similar setup was already used in Ref. [21].

The test setup shown in Fig. 1a is designed for application in a universal testing machine Zwick Z100. The connection to the machine table and the crossbar is realized via two punches centered to each other. The press force is transmitted via the end faces of the punches during the compressive cycles and via a step in the specimen and the clamp during tension. To ensure a centric force transmission, the connection of the specimen to the clamp is designed with a fit. The specimen shown in Fig. 1b is rotationally and plane symmetric and consists of three different diameters. The testing section in the middle of the specimen is cylindrical with a diameter of ∅ 8 mm and a height of 15 mm. The height-diameter-ratio is within the range given by Ref. [22] in order to prevent a buckling of the material. The transition to the fitting section is via a radius to ensure a good optical accessibility to the test section. The diameter ∅ 16 mm of the fitting section is a compromise between a small machining effort and a high step area. The latter is perpendicular to the rotational axis and responsible for the transmission of the tensile force. The clamped section has a diameter of ∅ 25 mm, which matches the diameter of the billets for the forming experiments.

During testing, the strain is measured with the optical strain measurement system GOM Aramis. Therefore, a stochastic dot pattern is deposited on the testing section of the specimens. The force necessary for the deformation of the specimen is measured with a load cell in the testing machine. The true stress is calculated from the measured forces and strains.

With this setup, specimens are tested in three load cycles, where the first and the third cycle have a compressive load and the second cycle has a tensile load. The deformation is strain-controlled with a speed of 0.01 s^{-1}. The strain control is provided by the software testXpert supplied with the testing machine. The reversal points are both symmetric and asymmetric.

The results of the cyclic plastification tests are shown in Fig. 2.

In curve A, a compressive strain of approximately 0.035 and a tensile strain of 0.025 were reached. The asymmetry of the curve offers an opportunity to prove the possibilities of fitting the numerical model. The experiments for the curves B, C and D were performed in a way that a symmetrical strain is reached in compressive and in tensile direction. Small deviations of up to 0.003 are due to the elasticity of the tools and slight inaccuracies in displacement measurement. In curve E, the highest strain was intended. In cycle III, the second compression cycle, a decrease of the strain can be recognized. This is due to a buckling of the specimen as a result of the high strain. The data of cycles I and II, however, can be used for the numerical model.

In cycle I, the first compression cycle, it can be seen that only very small deviations occur between the curves. This shows that stress and strain measurement are reliable and that homogeneous material properties are present in the samples. The distances between the curves in the cycles II and III show that kinematic hardening is occurring in the material. This proves that a solely isotropic hardening material model is not sufficient.
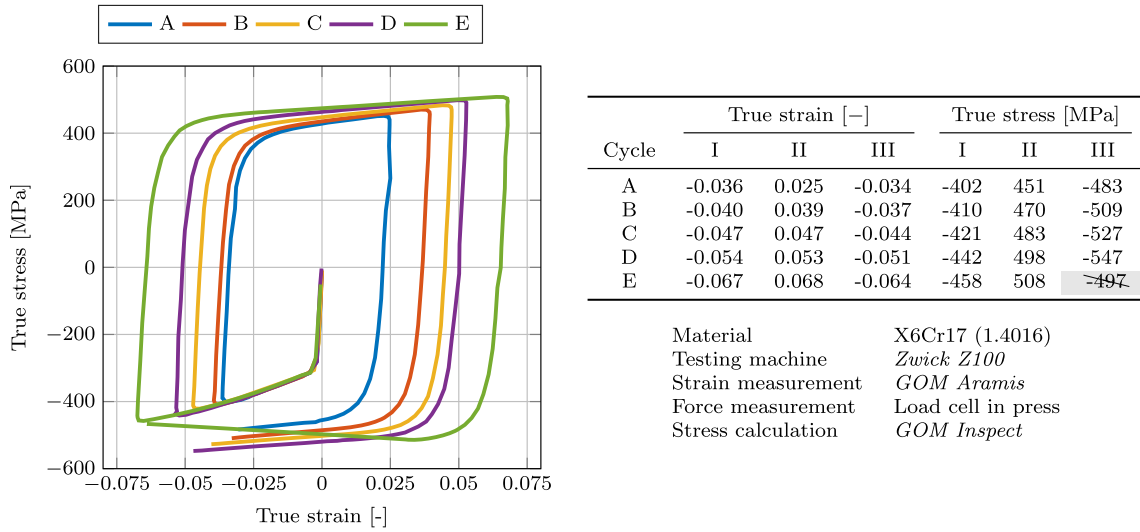
Fig. 2 Results of the compression-tension-compression tests. Stress–strain responses and reversal points

Cycle	True strain [−] I	II	III	True stress [MPa] I	II	III
A	-0.036	0.025	-0.034	-402	451	-483
B	-0.040	0.039	-0.037	-410	470	-509
C	-0.047	0.047	-0.044	-421	483	-527
D	-0.054	0.053	-0.051	-442	498	-547
E	-0.067	0.068	-0.064	-458	508	-497

Material	X6Cr17 (1.4016)
Testing machine	*Zwick Z100*
Strain measurement	*GOM Aramis*
Force measurement	Load cell in press
Stress calculation	*GOM Inspect*

2.2 Modeling – plasticity with combined hardening

To model the uni-axial elastic-plastic response of X6Cr17 (1.4016), the combined nonlinear isotropic/kinematic hardening (Chaboche [16]) model available in MSC Marc [23] was used. The elastic domain is defined by the yield function,

$$\Phi = \sqrt{\frac{3}{2}\boldsymbol{\sigma}_{\text{dev}}^{\text{red}} : \boldsymbol{\sigma}_{\text{dev}}^{\text{red}}} - [R + \sigma_{\text{y}}], \tag{1}$$

where $\boldsymbol{\sigma}_{\text{dev}}^{\text{red}}$ denotes the deviatoric part of the reduced stress, $\boldsymbol{\sigma}^{\text{red}} \stackrel{def}{=} \boldsymbol{\sigma} - \boldsymbol{X}$. In the latter, $\boldsymbol{\sigma}$ and $\boldsymbol{X}$ denote the Cauchy stress and backstress, respectively. Furthermore, σ_{y} is the initial yield stress and R is an isotropic hardening parameter defined as, $R = R_\infty[1 - e^{-b\kappa}]$. R_∞ is the maximum size of the elastic domain, κ is the accumulated equivalent plastic strain and b is the rate of change of the elastic domain. Finally, the evolution of the plastic strain $\boldsymbol{\epsilon}^{\text{p}}$ and backstress is determined by the equations,

$$\dot{\boldsymbol{\epsilon}}^{\text{p}} = \dot{\lambda}\frac{\partial\Phi}{\partial\boldsymbol{\sigma}}, \quad \dot{\boldsymbol{X}} = \left[\frac{C}{R + \sigma_{\text{y}}}\boldsymbol{\sigma}^{\text{red}} - \gamma\boldsymbol{X}\right]\dot{\lambda}, \tag{2}$$

where λ is the plastic multiplier and, C and γ are kinematic hardening parameters. Equations (1) and (2) comprise the system of equations from which the internal variables of the local constitutive problem at hand are determined after time discretization.

Identification of the constitutive model parameters was based on force-displacement data from the uni-axial compression-tension-compression tests described in Sect. 2.1. Young's modulus, Poisson's ratio and the initial yield stress were set to, $E = 210000$ MPa, $\nu = 0.28$ and $\sigma_{\text{y}} = 263.74$ MPa, in accordance with Ref. [15]. The four-dimensional set of remaining parameters for calibration was $\underline{x} = \left\{ R_\infty \ b \ C \ \gamma \right\}$.

The calibration was performed using the two-dimensional axisymmetric FE-model depicted in Fig. 3. The FE-model was developed in MSC Marc. Only half of the specimen from the experiments was considered due to symmetry. The model featured 374 bi-quadratic (8-node) quadrilaterals with reduced (2×2) integration. Symmetry boundary conditions were applied at the left and bottom boundaries. The measured displacement[1] from the experiment in the axial direction was prescribed at the right boundary and the total reaction force ($\overline{F}^{\text{sim}}$) obtained from the FE-model on that boundary was calibrated against the measured force ($\widehat{F}^{\text{exp}}$) from the experiment.

---

[1] The end-displacements of the specimen that were used as input to the calibration were extracted from measured displacements of the crossbar, see Fig. 1a, by removal of any tool elasticity included in the raw data. The validity of the calibrated parameters was verified on the corresponding stress-strain problem at a material point, i.e. that the combined hardening model was able to capture the true stress-strain response from the experiments provided in Fig. 2.
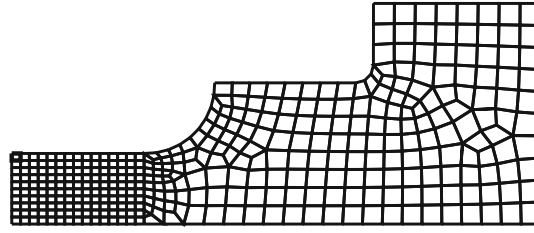
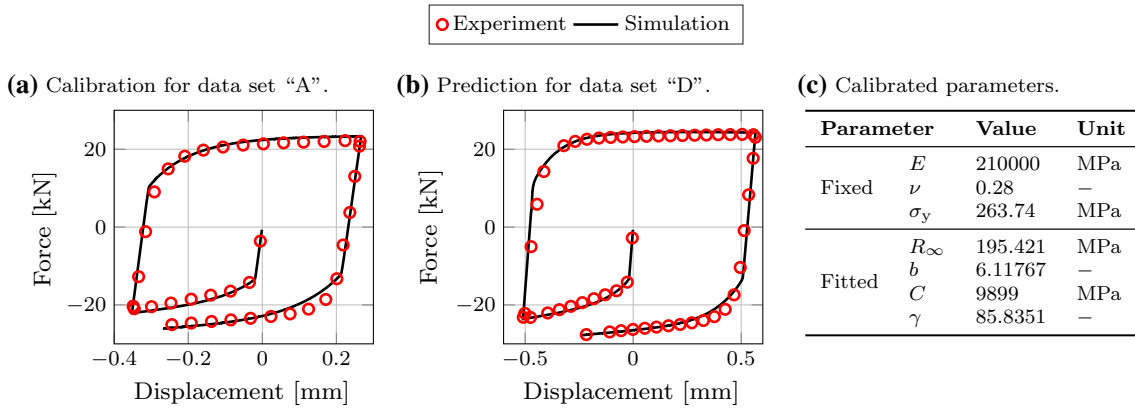**Fig. 3** Axisymmetric FE-model used in the calibration of the combined hardening constitutive model

○ Experiment —— Simulation

(a) Calibration for data set "A". **(b)** Prediction for data set "D". **(c)** Calibrated parameters.

Parameter		Value	Unit
	E	210000	MPa
Fixed	ν	0.28	–
	σ_y	263.74	MPa
	R_∞	195.421	MPa
Fitted	b	6.11767	–
	C	9899	MPa
	γ	85.8351	–

Fig. 4 Calibrated and predicted responses of the combined hardening model

The error function between simulated and measured forces was defined as

$$E_F\left(\underline{x}\right) = \sqrt{\sum_{i=1}^{N_i}\left[\frac{{}^i\overline{F}^{\,\text{sim}}\left(\underline{x}\right) - {}^i\widehat{F}^{\,\text{exp}}}{\Delta F^{\text{exp}}}\right]^2}, \tag{3}$$

where i denotes the data point and, $\Delta F^{\text{exp}} = \max_i {}^i\widehat{F}^{\,\text{exp}} - \min_i {}^i\widehat{F}^{\,\text{exp}}$. The problem of finding $\underline{x}$ that minimizes the error function defined in Eq. (3) was solved via optimization. In particular, a bounded conjugate gradients method, implemented in MATLAB via the function `fminsearchbnd` (see [24]), was used. The parameter identification procedure described above was implemented on data set "A", see Fig. 2. The calibrated parameters are provided in Fig. 4c and the corresponding force-displacement responses for data sets "A" and "D" are illustrated in conjunction to the responses from the experiments in Fig. 4a, b. The results show an accurate fit for data set "A" and an excellent prediction of the experimentally measured material response for data set "D". From the values of the calibrated parameters in Fig. 4c, it can be deduced that approximately 37% was the amount of kinematic hardening obtained in the calibration.

To be able to perform an evaluation of the effect of the chosen constitutive model in subsequent full-forward extrusion FE analyses (see Sect. 3.2), calibration of the isotropic part of the considered combined hardening model was also performed. In this regard, the kinematic hardening parameters were set to $C \approx 0$ [MPa] and $\gamma = 0$. The two-dimensional set of remaining parameters for calibration was $\underline{y} = \{R_\infty, b\}$. Identification of these parameters was performed only on the first compression cycle of data set "$\overline{A}$", due to the inability of a pure isotropic constitutive "law" to capture unloading. The obtained force-displacement fit for data set "A" and the predicted force-displacement response with the calibrated parameters for data set "D" are shown in Fig. 5a, b, respectively. As expected, the response from the experiment is well captured in the calibrated first compression cycle, whereas a non-satisfactory agreement with the experiments is at hand for the tension-compression cycles that follow.
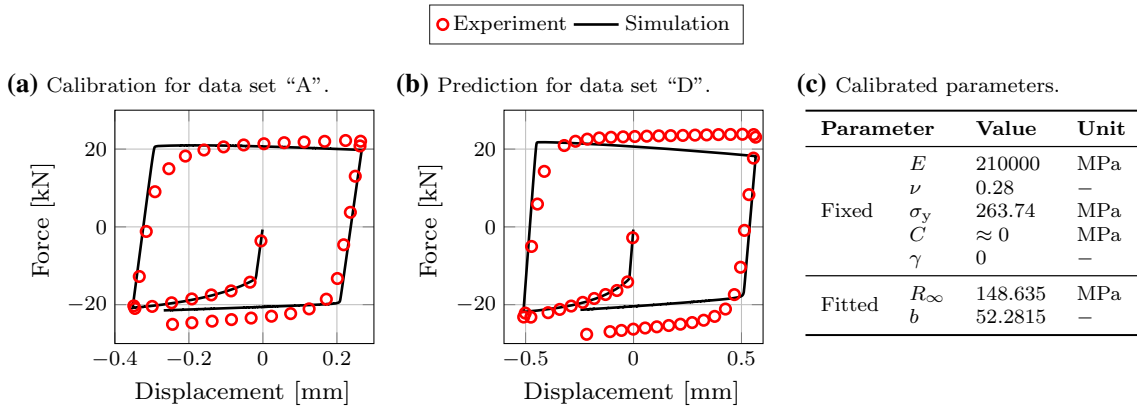
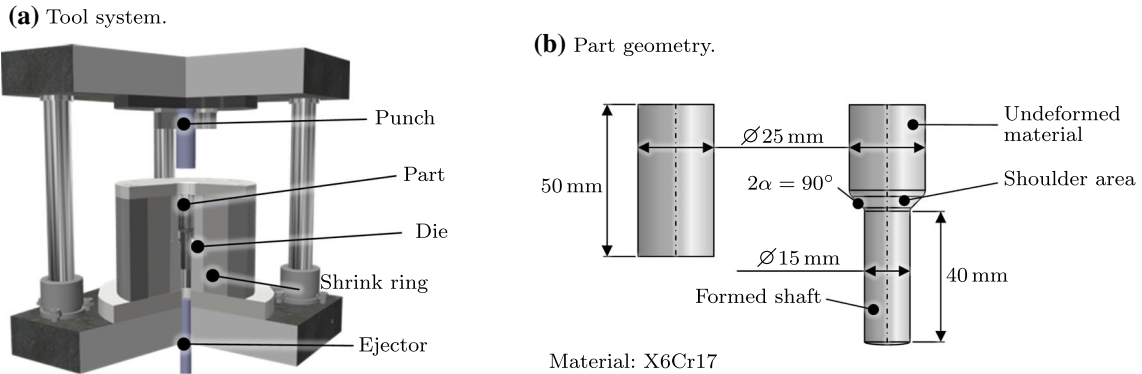**Fig. 5** Calibrated and predicted responses of the isotropic part of the combined hardening model

Fig. 6 Forward rod extrusion experiments

3 Forming phase: full-forward extrusion

3.1 Experiment – residual stress measurement

For the investigation of residual stress related issues in the forward rod extrusion of stainless steels, a representative forming process is carried out. The tool system and the resulting part geometry of the experiments are shown in Fig. 6.

Forming takes place with the tool system shown in Fig. 6a in a hydraulic press type *Lasco TZP 400* with a maximum press force of 4000 kN. The part geometry is specified by the die made of tool steel ASP2012 (EN: HS 2-2-2, DIN: 1.3397). In order to limit the radial expansion of the die during forming, it is pressed into a shrink ring made of hot working steel X38CrMoV5. The press force is transmitted into the billet via a punch made of powder-metallurgic high-speed steel Vanadis 23 (EN: PMHS6-5-3, DIN: 1.3395). For a centric force transmission and to prevent a crash of the tool elements, the punch is mounted within a column guide frame. The formed parts are ejected in opposite direction to the punch with an ejector.

Due to its industrial relevance, the ferritic stainless steel X6Cr17 (DIN: 1.4016) is used for the forming experiments. The produced geometry is shown in Fig. 6b. From rods with a diameter of 25 mm, billets are cut with a length of 50 mm. The billets are coated with a tribological system consisting of iron-III-oxalate as lubricant carrier layer and molybdenum disulphide (MoS 2) as lubricant. Forming takes place in the above-mentioned die with a die opening angle of $2\alpha = 90°$, which is in the range of angles used in industry. The target diameter is 15 mm, which corresponds to an equivalent plastic strain of $\bar{\epsilon} = 1.02$.

During forming, the billet is subjected to the punch force, thus exceeding the yield stress and causing the material to flow along the die contour. The force-displacement curve during forming and the resulting material flow pattern in the formed component are shown in Fig. 7.

The force–displacement curve in Fig. 7a shows a steep increase in force for the first 5 mm of punch displacement. During this non-stationary start-up, the static friction is overcome and the die shoulder is filled
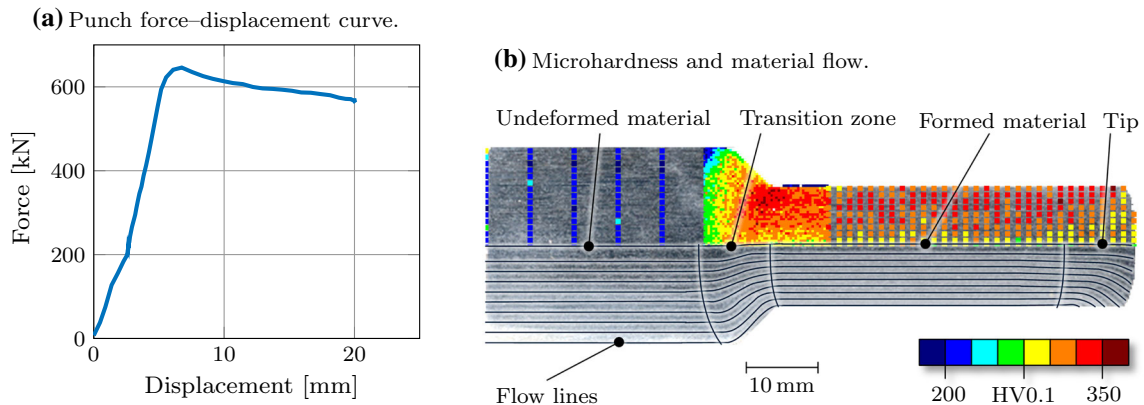
(a) Punch force–displacement curve.

(b) Microhardness and material flow.

Fig. 7 Punch force–displacement curve and, microhardness and material flow data

with material. Thereby the maximum force of 644 ± 2 kN is reached. After the material has passed the die land, the quasi-stationary extrusion takes place and the punch force decreases linearly. This is due to a linear reduction of the contact area between billet and die in the cylindrical area above the shoulder. At a displacement of 20 mm, a formed shaft length of approximately 42 mm is reached, which corresponds to the targeted geometry. After raising the punch, the part is ejected from the die against the forming direction.

The microhardness and the material flow in the formed specimens are shown in the longitudinal cut in Fig. 7b. The samples are prepared by cutting, grinding and polishing for hardness measurement and microstructure analysis. The microhardness is measured with the instrumented indentation test according to Ref. [25] using a *Fischerscope® HM2000*. Etching with nitric and hydrochloric acid reveals the grain boundaries and therefore allows the determination of grain orientations. In the non-deformed material, a homogeneous hardness distribution with values of 220 HV is present. The grains are slightly elongated, which can be traced back to the production of the rods. In the transition zone, the die shoulder causes a deflection of the material, leading to a radial compression and an axial elongation of the grains. This inhomogeneous velocity field significantly contributes to the development of residual stresses [26]. In addition, work hardening of the material to about 330 HV is observed. Along the formed shaft, microhardness, grain shape and grain size distributions are homogeneous due to the quasi-stationary process sequence. In the tip, the material in the core shows a reduced hardness of 283 HV, while the surface still has values up to 350 HV. This is due to the non-stationary initial stage of the process, where the end face of the billet is pressed through the die shoulder. This also leads to flow lines ending in the outer surface, which also indicates inhomogeneous material properties and residual stresses.

The quantification of the residual stresses within the formed parts is carried out via X-ray diffraction (XRD). The reflected angle of the X-ray beam allows the determination of lattice plane distances, which are sensitive to mechanical stresses [27]. This method allows a non-destructive measurement of both load and residual stresses [28]. The measurement takes place on an X-ray diffractometer type Seifert XRD 3003 with the χ-method according to DIN EN 15305 [29]. The residual stresses are measured on the formed shaft both in axial and tangential direction. The results are shown in Fig. 2.

In axial direction, there are distinct tensile residual stresses with a maximum value of 310 MPa, while low tensile stresses are present in tangential direction, which vanish towards the tip of the specimen. In the area close to the die shoulder, unsteady residual stresses are present due to the inhomogeneous material flow within the shoulder area. Adjacent to this is an approximately 20 mm long area in which a homogeneous stress state is present due to the quasi-stationary extrusion sequence. Towards the tip, an influence of the non-stationary start-up of the forming process is seen in the unsteady stress state.

From the literature, a constant axial residual stress state is expected starting at a distance of 7.5 mm from the shoulder – corresponding to half the diameter of the shaft [30]. This expectation was confirmed in Ref. [15], where constant axial and tangential residual stresses were observed between 8 mm from the shoulder and 5 mm from the tip in non-ejected parts. The ejection from the die after forming results in the residual stress state shown in Fig. 8. The residual stress change during ejection is caused by the movement of the formed shaft through the die land, whose diameter is reduced due to springback [31].

The identified residual stress state with tensile near-surface stresses is due to the inhomogeneous material flow while passing the shoulder in the forming die. A non-uniform velocity field with higher axial material flow
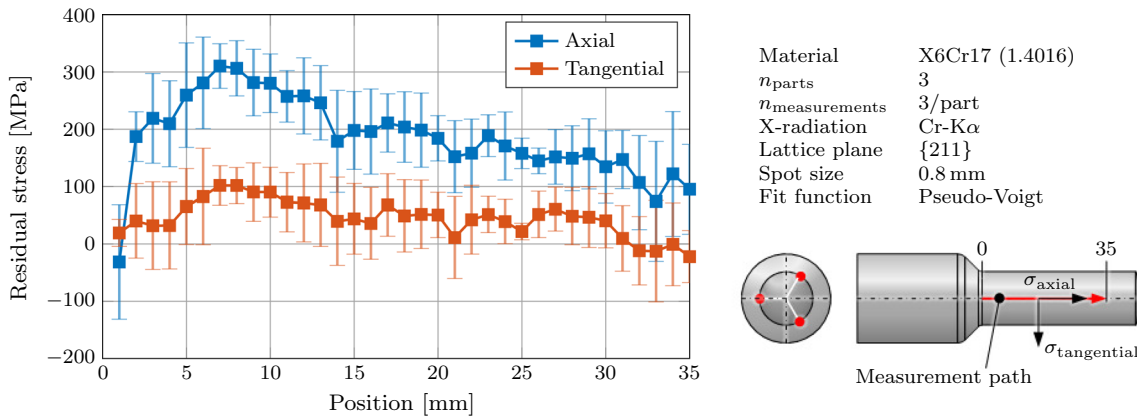
Fig. 8 Residual stresses on the surface of a forward rod extruded specimen

Table 1 Material parameters used in forming simulations

Part	Material	Parameters
Workpiece	X6Cr17 (1.4016)	See Figs. 4c and 5c
Die	ASP2012	$E = 220000\,[\text{MPa}], \nu = 0.30$
Reinforcement	X37CrMoV5	$E = 210000\,[\text{MPa}], \nu = 0.30$
Punch/ejector	Rigid	–
Top/bottom plates		

next to the specimens surface leads to the presence of tensile residual stresses in the surface and compressive residual stresses in the core. This residual stress state is common for forward rod extrusion with the presented die geometry and process design [32]. A comparison to the hardness distribution in Fig. 7 shows that the residual stresses are more sensitive to peripheral phenomena and that an area with constant properties is generated with this setup.

3.2 Simulation – residual stress prediction

The forming experiment outlined in Sect. 3.1 was simulated by a finite strain FE-model developed in the commercial FE-code MSC Marc, see Fig. 9. The model was comprised of three continuum parts: reinforcement ring, die and workpiece, and four rigid bodies representing the punch, the ejector and the lower and upper base plates, cf. Fig. 6. The dimensions of all the parts are detailed in Sect. 3.1. Furthermore, the reinforcement ring and the die were modelled as linear elastic, whereas the built-in MSC Marc (Chaboche) combined nonlinear isotropic/kinematic hardening model was used for the workpiece. For the latter, two cases were considered, one with combined hardening and one with the isotropic hardening part of the combined hardening model. The calibrated parameters for both cases are provided in Sect. 2.2. The values of the material parameters for all the three parts are summarized in Table 1. The FE-model was discretized via 8005 bilinear quadrilateral axisymmetric elements with full (2×2) integration. The majority of the elements was dedicated to the workpiece in a process adapted mesh towards the bottom edge of the workpiece, see Fig. 9b. The particular mesh design allows for material flow through the shoulder of the die without excess element distortion, such that remeshing and its accompanying sources of numerical errors are avoided.

Normal and frictional contact constraints between all the parts were enforced via penalty method and a node-to-segment contact discretization. The "shear (bilinear)" friction model in MSC Marc was used to model friction between the corresponding parts of the model. The friction factor between the workpiece and die was set to $\mu_{\text{wd}} = 0.126$, as measured in experiments. To reach the experimentally determined pressure exerted between the reinforcement ring and die, the friction factor between the pertinent parts was set to $\mu_{\text{rd}} = 0.06$. A factor $\mu_{\text{rc}} = 0.10$ was used for the friction between all the rigid bodies and the corresponding continuum parts, as proposed in Ref. [33] for extrusion processes.

Simulations with and without ejection of the workpiece were performed in three steps. Symmetry boundary conditions were enforced along the axis of rotational symmetry during all the three steps. In the first step, the
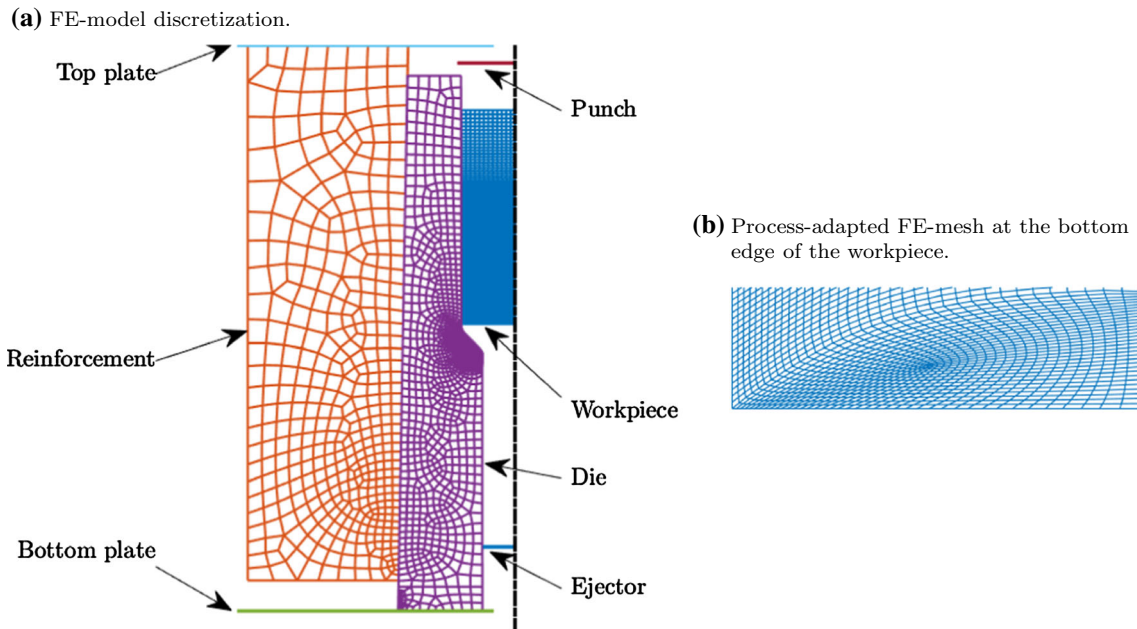
(a) FE-model discretization.

(b) Process-adapted FE-mesh at the bottom edge of the workpiece.

Fig. 9 Axisymmetric FE-model for full-forward extrusion simulations

reinforcement ring with a 5‰ oversize (equates to some 0.125[mm] radial distance) was displaced downwards towards the die via contact with the top rigid body/plate. Forming of the workpiece was performed at the second step, during which the workpiece was displaced 22[mm] (from the undeformed position illustrated in Fig. 9a) downwards via contact with the corresponding rigid body/punch. During this step, the radial displacement of the reinforcement was restrained at its leftmost boundary (see Fig. 9a), such that the pressure developed betweeen the reinforcement and die at the end of the first step is preserved. In the case without ejection, unloading was the third step by removal of contacts between the workpiece and die as well as the punch. Whilst, in the case with ejection, the third step was comprised of some 60[mm] upwards displacement of the workpiece (starting from its position at the end of forming) via contact with the corresponding bottom rigid body/ejector, until no pressure was exerted between the workpiece and die.

Forming simulations with the setting described above were performed using the combined hardening model calibrated in Sect. 2.2 for the material of the workpiece. Measured and numerically determined residual stresses at the end of the third step are compared in Fig. 10. The pertinent stresses at the surface nodes of the workpiece were determined via the "nodal averaging" extrapolation option in MSC Marc. Smooth axial and tangential residual stress distributions along the measurement path indicated in Fig. 8 are obtained. Both residual stress components are overpredicted in the case without ejection, see Fig. 10a, b. This effect is more pronounced for the axial stress component. However, the overall trend of the two curves is in agreement with the shape of the corresponding measured stress distributions. This does not hold for both stress components in the case with ejection, see Fig. 10c, d. Namely, rather tortuous residual stress distributions are obtained. The predicted axial residual stresses are not in agreement with the corresponding experimentally measured values. A better agreement (on average) with the experiments is at hand for the tangential stresses.

To investigate the effect of the material model of the workpiece on the predicted residual stresses, the forming simulations were repeated using a pure isotropic hardening model for the workpiece, as calibrated in Sect. 2.2. Results for the cases without and with ejection are depicted in Fig. 11. The agreement with the experimentally measured axial and tangential residual stresses is nearly exact for the case without ejection, as shown in Fig. 11a, b, respectively. The same holds for the axial stress component in the case with ejection, see Fig. 11c, and the tangential stress component in the region 17–35 [mm] along the measurement path.
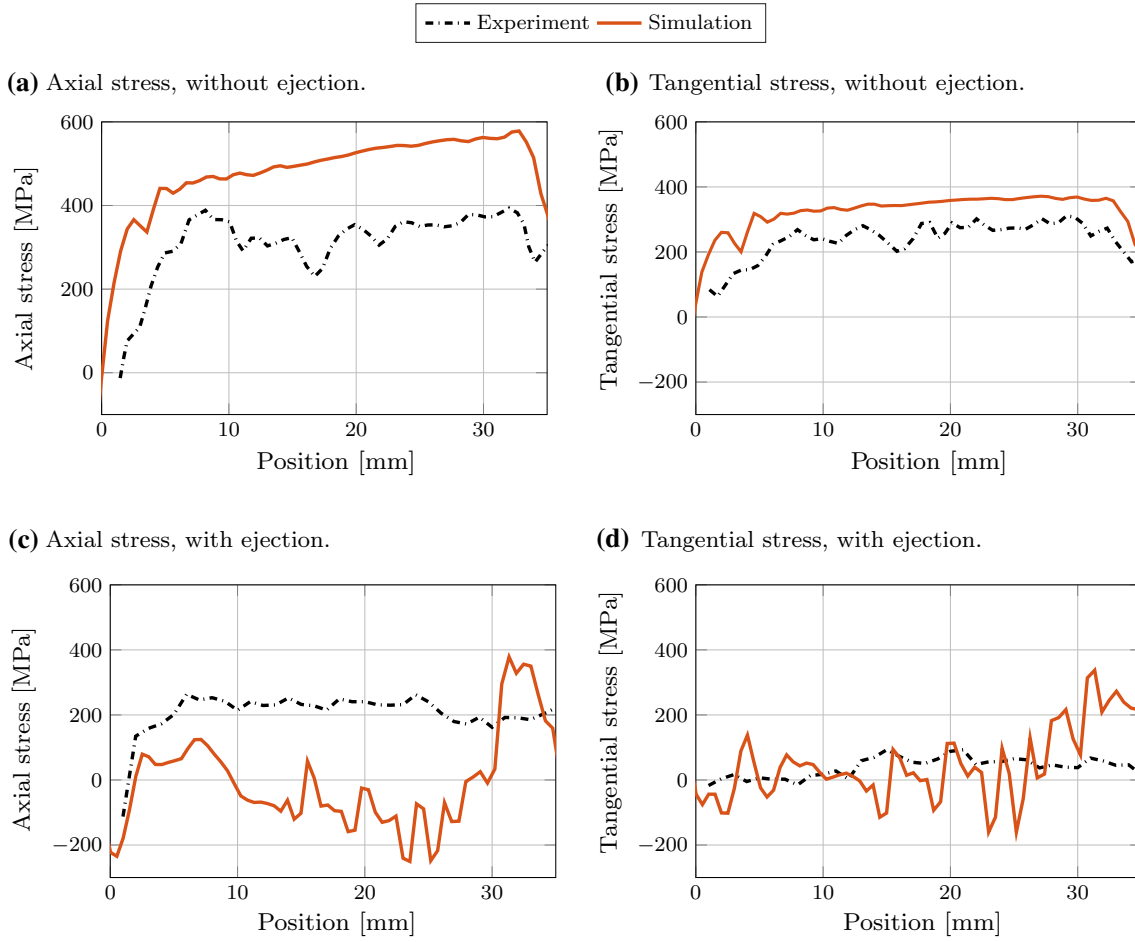
Fig. 10 Comparison of measured against predicted residual stresses for the case of combined hardening. The position is measured with respect to the measurement path indicated in Fig. 8. The experimental results in the case without ejection were taken from Ref. [15])

4 Operating phase: effect of forming-induced residual stress

A qualitative study of the effect of residual stresses induced by full-forward extrusion on fatigue life of the workpiece by means of uncoupled multiscale FE-simulations is described in this section. At the microscale, the scale of the grains, a gradient enhanced crystal plasticity model was used [20,34–36]. The microscale was coupled via numerical homogenization to the macroscale.

In the following, the model in the microscale is shortly described. The kinematic, constitutive and governing equations are given within the context of small strains. Thus, the strain $\boldsymbol{\varepsilon}$ is defined as the symmetric gradient of a displacement field $\boldsymbol{u}$ for all points $\boldsymbol{x}$ in a body $\mathcal{B}$. The strain is additively split in elastic $\boldsymbol{\varepsilon}^e$ and plastic parts $\boldsymbol{\varepsilon}^p$,

$$\boldsymbol{\varepsilon} = \nabla^{\text{sym}} \boldsymbol{u} = \boldsymbol{\varepsilon}^e + \boldsymbol{\varepsilon}^p. \tag{4}$$

In single crystal plasticity, the plastic strains are modelled as the sum of shear deformations in all present slip systems. A face centred unitcell has 12 independent slip systems. With the slip directions $\boldsymbol{s}^a$ and the normal of the corresponding slip system $\boldsymbol{m}^a$ in slip system a, the plastic strains $\boldsymbol{\varepsilon}^p$ are formulated as

$$\boldsymbol{\varepsilon}^p = \sum_a \gamma^a \left[\boldsymbol{s}^a \otimes \boldsymbol{m}^a \right]^{\text{sym}} = \sum_a \gamma^a \boldsymbol{p}^a, \tag{5}$$

where $\boldsymbol{p}^a$ denotes the so-called Schmid tensor and γ^a is the scalar-valued amount of slip in system a. The gradient enhancement of the model is motivated by means of the Nye tensor, a measurement of the geometrically
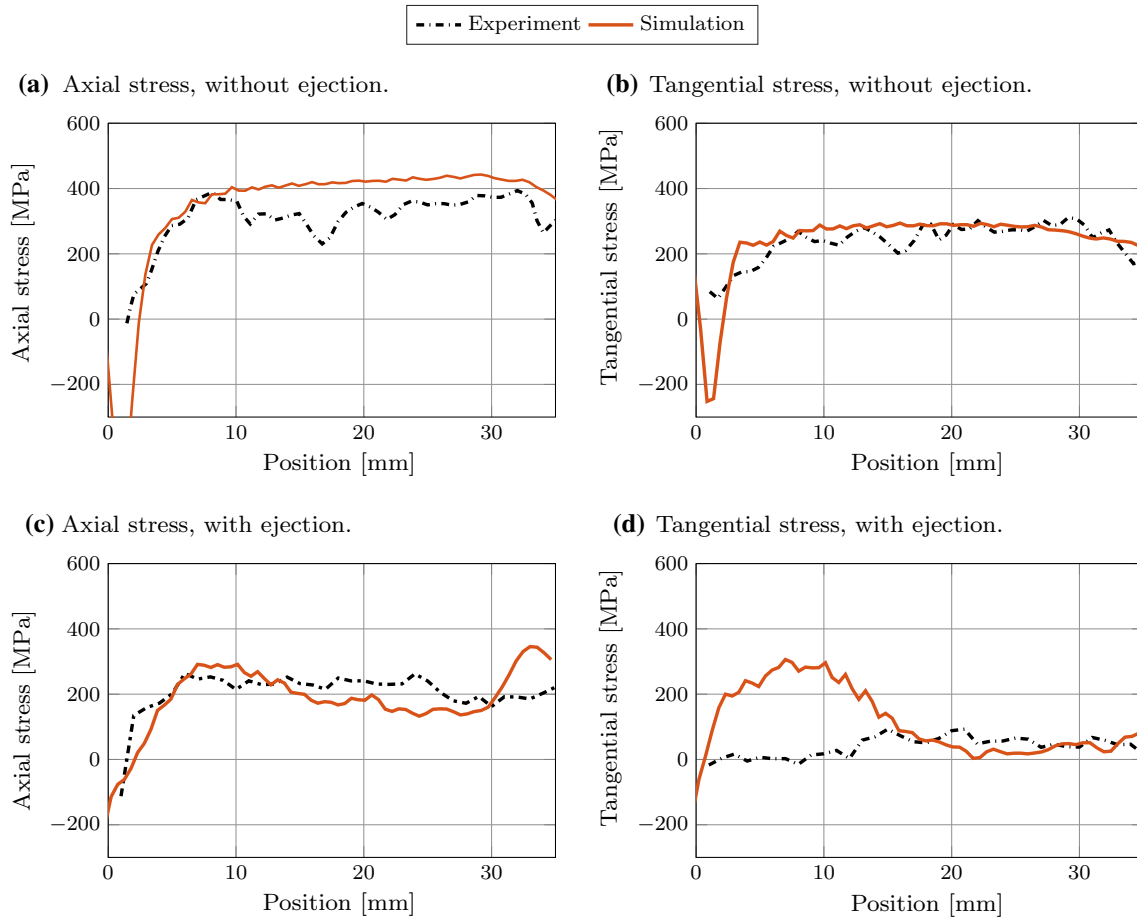
Fig. 11 Comparison of measured against predicted residual stresses for the case of pure isotropic hardening. The position is measured with respect to the measurement path indicated in Fig. 8. The experimental results in the case without ejection were taken from Ref. [15])

necessary dislocation state at a material point. It follows that the screw $\alpha_a^{\parallel}$ and edge $\alpha_a^{\perp}$ dislocation densities depend on the gradient of the slips γ^a tangential to the slip system,

$$\alpha_a^{\parallel} = \boldsymbol{l}^a \cdot \nabla \gamma^a, \quad \alpha_a^{\perp} = -\boldsymbol{s}^a \cdot \nabla \gamma^a. \tag{6}$$

The line vector $\boldsymbol{l}^a$ is a bi-normal on the slip direction and the slip system normal defined as $\boldsymbol{l}^a = \boldsymbol{m}^a \times \boldsymbol{s}^a$. The free energy is defined according to Ref. [34] depending on the elastic strain and all dislocation densities, $\boldsymbol{\alpha} = \{\alpha_1^{\parallel}, ..., \alpha_n^{\parallel}, \alpha_1^{\perp}, ..., \alpha_n^{\perp}\}$, as

$$\Psi\left(\boldsymbol{\varepsilon}^e, \boldsymbol{\alpha}\right) = \frac{1}{2}\boldsymbol{\varepsilon}^e : \mathcal{C}^e : \boldsymbol{\varepsilon}^e + \frac{1}{2}\pi_0 \ell \sum_a \left[\left[\alpha_a^{\parallel}\right]^2 + \left[\alpha_a^{\perp}\right]^2\right]. \tag{7}$$

$\mathcal{C}^e$ denotes the fourth-order elasticity tensor, in the case of face centred unitcells with cubic symmetry depending on the Young's modulus E, shear modulus G and Poisson's ratio ν. The gradient enhancement comes with the introduction of the energetic length scale ℓ and π_0 is introduced as a critical shear stress. On the grain boundaries, there is an additional term that enters the free energy depending on the incompatibility of the plastic strains over the grain boundary between grains A and B with the normal $\boldsymbol{n}$ pointing from grain A to grain B [36]. It is formulated by means of the grain boundary burgers tensor,

$$\mathcal{G} = \left[\left[\boldsymbol{\varepsilon}_B^p - \boldsymbol{\varepsilon}_A^p\right] \otimes \boldsymbol{n}\right] : \boldsymbol{e}, \tag{8}$$

Table 2 Material parameters for the microscopic model

Parameter	Value	Unit
E	130830	MPa
μ	116600	MPa
ν	0.369	–
τ_0	130	MPa
h_0	100	MPa
ℓ	24	μm
$\dot{\gamma}_0$	0.01	s^{-1}
q	1.4	–
λ_{gb}	10000	Nm^{-1}

where e denotes the third-order Levi-Civita tensor. The additional energy on the grain boundaries is quadratic in the grain boundary burgers tensor and reads

$$\Psi^{\mathrm{gb}} = \frac{1}{2}\lambda_{\mathrm{gb}}\mathcal{G} : \mathcal{G}, \tag{9}$$

introducing a penalty parameter λ_{gb}. The balance equations that follow are formulated in terms of the energetically conjugated quantities: elastic strain $\boldsymbol{\varepsilon}$ and stress $\boldsymbol{\sigma} = \partial\Psi/\partial\boldsymbol{\varepsilon}^e$, slips γ^a and corresponding microscopic stress π^a, as well as the gradient on the slips $\nabla\gamma^a$ and microscopic stress vector $\boldsymbol{\xi}^a = \partial\Psi/\partial\nabla\gamma^a$. The latter pair enters the formulation due to the gradient enhancement. The balance equations are the standard balance of linear momentum neglecting body forces, solved for a displacement field $\boldsymbol{u}$, and a micro force balance solved for all slip systems,

$$\mathrm{div}\,(\boldsymbol{\sigma}) = \mathbf{0}, \quad \mathrm{div}\,(\boldsymbol{\xi}^a) + \tau^a - \pi^a = 0. \tag{10}$$

Due to the gradient enhancement, the total number of degrees of freedom at each point $\boldsymbol{x}$ is 15, i.e. 12 slips and 3 displacements. The set of equations is completed by a constitutive equation for the crystallographic slips γ^a. From a Norton-Hoff approximation followed by a regularization [35] to improve numerical stability, the shear stress related to a slip rate follows as

$$\pi^a = \left[\pi_0 + g^a\right] \tanh\left(\frac{\dot{\gamma}^a}{\dot{\gamma}_0}\right). \tag{11}$$

Here, π_0 denotes the critical Schmid stress and $\dot{\gamma}_0$ is a reference slip rate. Hardening is formulated in a way to consider self- and latent hardening with the self-latent-ratio q, the hardening slope h_0, and is given by

$$g^a = \sum_a h_0 \left[q + [1 - q]\,\delta^{ab}\right]\dot{\gamma}^b. \tag{12}$$

In the following, the simulation setting is summarized shortly. In this regard, the three-dimensional RVE depicted in Fig. 12 was considered under periodic boundary conditions. The RVE was comprised of 12 grains, each highlighted by a different color in the figure, depending on the orientation of lattice structure. The grains were considered elongated towards the forming direction (i.e. the Z-axis in the figure), thus resembling, in a qualitative manner, the granular microstructure of an extruded specimen, e.g. the round bar illustrated in Fig. 12. This feature allowed discretization of the RVE by only one row of finite elements in the extrusion direction. The material parameters are given in Table 2. The model was implemented in the finite element library Deal.ii [37].

The RVE was sequentially subjected to two strain states. The first one corresponded to a strain state "representative" of the full-forward extrusion process, which essentially generated a residual strain state at the (macroscale) integration point that the RVE is assumed to reside. To determine the strain state that acted on top of the aforementioned one, the solid bar depicted in Fig. 12 was subjected quasi-statically to the bending force F with magnitude that lied macroscopically in the elastic regime. The strain state at the integration point with the maximum effective von Mises stress comprised then the second "load" on the RVE and was imposed as amplitude on the RVE in 10 sinusoidal cycles.

Subsequently, the effective (macroscale) response was determined from homogenization over the RVE as described in Ref. [20]. The response in terms of effective von Mises stress and equivalent strain measures is
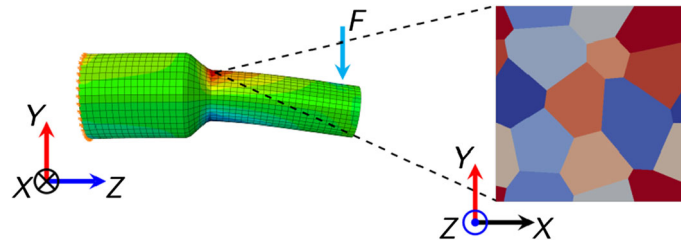
Fig. 12 Setting for uncoupled multiscale modeling. The colormap in the bar represents effective von Mises stress, whereas different colors in the RVE stand for the grains each with its own orientation of lattice structure. Measuring point corresponds to the point of maximum von Mises stress for a macroscopic bending loading
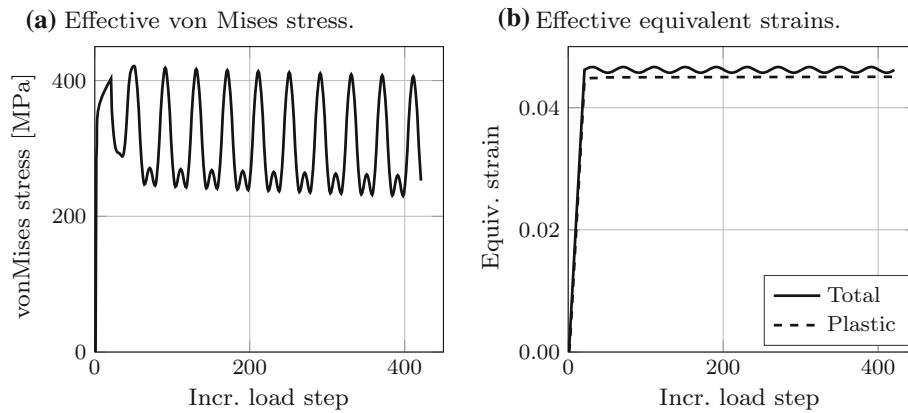
(a) Effective von Mises stress.   **(b)** Effective equivalent strains.

Fig. 13 Effective (macroscale) response obtained from homogenization over the RVE

given in Fig. 13. The slight decrease in macroscopic von Mises stress is partly due to the particular formulation of the crystal plasticity model. However from Fig. 14 it can be seen that the plastic strain rate decreased significantly over the cycles resulting in new equilibrium that will be reached after a certain number of cycles. Accompanying is a reduction of residual stress. Due to the particular crystal plasticity formulation, the exact number of cycles to reach this point will be underestimated but the trend can be determined.

5 Discussion

To be able to more accurately model full-forward extrusion and consequently arrive at improved prediction of forming induced residual stresses, a combined nonlinear isotropic/kinematic hardening model was calibrated for X6Cr17 (1.4016) steel, see Sect. 2.2. For this purpose, five uniaxial stress experiments were performed, each featuring one cycle in compression-tension-compression such that transient phenomena such as the Bauschinger effect became apparent. From the values of identified material model parameters, a non-negligible amount ($\approx 37\%$) of kinematic hardening was found present. In addition, the isotropic part of the considered combined hardening model was also calibrated on the same data, in order to evaluate the effect of the choice of the constitutive model of the workpiece on the predicted forming induced residual stresses.

Results from a full-forward rod extrusion experiment in Sect. 3.1 were used for the validation of an FE-model of the pertinent forming process adopting for the material of the workpiece a combined isotropic/kinematic hardening model as well as the isotropic hardening part of the combined hardening model, see Sect. 3.2. Results from forming simulations with and without modeling of the ejection phase revealed that the FE-model with isotropic hardening was able to satisfactorily capture the experimentally measured axial and tangential residual stresses, see Fig. 11.

Furthermore, the residual stress predictions from combined hardening modeling of the workpiece were found in Sect. 3.2 of inferior quality than the corresponding ones obtained with isotropic hardening modeling. At a first glance, this may not be expected, especially for the case of forming with modeling of the ejection phase, where unloading of the workpiece is presumed to take place. The reasons for this outcome need to be investigated in future work.
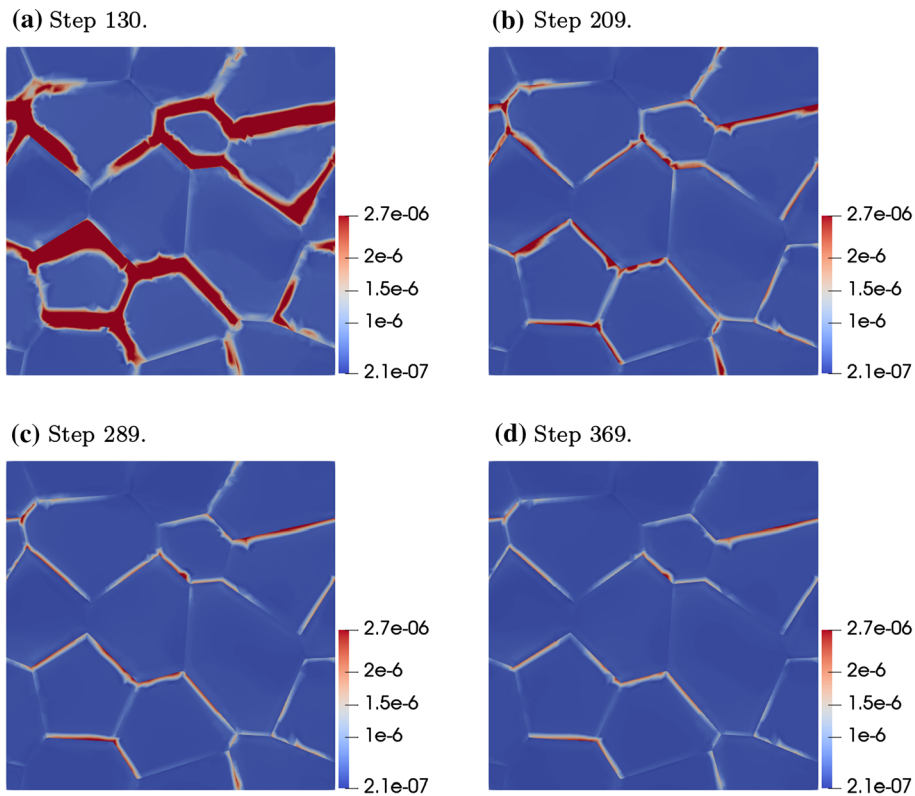
(a) Step 130.   **(b)** Step 209.

(c) Step 289.   **(d)** Step 369.

Fig. 14 Equivalent plastic strain rate at different increment loading steps with accompanying reduction in residual stress (snapshots taken for the same angle at four different load cycles)

In the qualitative study of the effect of residual stresses on the fatigue life of a workpiece in Sect. 4, the effective (macroscale) equivalent plastic strain induced by a forming-like strain state was found rather constant during a subsequent macroscopically elastic cyclic loading, see Fig. 13b. Moreover, the effective (macroscale) von Mises stress exhibited a decreasing trend over the incremental loading steps, see Fig. 13a. Thus, an overall elastic material response was obtained macroscopically. However, the plasticity induced by the forming (strain state) still manifested itself in regions such as the grain boundaries. These are regions where over continued cyclic loading even below the (macroscopic) fatigue limit, material failure similar to a high cycle fatigue might initiate from.

The above uncoupled multiscale modeling comprises a precursor to scheduled fully coupled multiscale simulations. More specifically, an effective (i.e. phenomenological) material constitutive model will be developed based on simulations on a number of RVE realizations of the granular microstructure of the considered material. In particular, the RVEs will be prestressed with the residual stress state from forming. The developed effective model will be used as a constitutive driver in macroscale simulations under cyclic loading, that will provide with a tool for numerical evaluation of the effect of residual stresses on fatigue life of a formed component.

6 Conclusions

To study the effect of constitutive model on the predicted forming induced residual stresses on a workpiece made of X6Cr17 (1.4016) steel, a combined nonlinear isotropic/kinematic hardening model as well as the isotropic hardening part of the model were calibrated. The parameter identifications were performed on uniaxial stress experiments featuring compression-tension-compression cycles, such that cyclic plasticity effects became apparent. The combined hardening model under the fitted parameters was able to accurately capture the measured uniaxial elastic-plastic material response at finite strain amplitudes.

The above-mentioned constitutive models were used in full-forward rod extrusion simulations with and without modeling of the ejection phase. The results from the FE-modeling indicated that pure isotropic harden-

ing modeling of the workpiece results in accurate prediction of residual stresses and modeling thus the kinematic hardening may be viewed as unnecessary. However, further research is required into material modeling effects on forming induced residual stresses, especially for the case that the ejection phase is modeled.

In the final contribution of the paper, the effect of residual stresses induced by forming on the fatigue life of a workpiece during operation was qualitatively investigated via microscale RVE simulations featuring gradient crystal plasticity. Although the effective (homogenized) response obtained from the RVE indicated that no further plasticity events take place after forming, small scale plastic response at grain boundaries was identified within the RVE which led to reduction of residual stress; a material "failure" mechanism which was viewed analogous to fatigue.

Compliance with ethical standards

Conflict of interest The authors declare that they have no conflict of interest.

References

1. McClung, R.C.: A literature survey on the stability and significance of residual stresses during fatigue. Fatigue Fract. Eng. Mater. Struct. **30**(3), 173–205 (2007). https://doi.org/10.1111/j.1460-2695.2007.01102.x
2. James, M., Hughes, D., Chen, Z., Lombard, H., Hattingh, D., Asquith, D., Yates, J., Webster, P.: "Residual stresses and fatigue performance". In: Engineering Failure Analysis. Papers presented at the 22nd meeting of the Spanish Fracture Group (Almargro, Spain, March 2005), pp. 384–395 (2007) https://doi.org/10.1016/j.engfailanal.2006.02.011.http://www.sciencedirect.com/science/article/pii/S1350630706000562
3. Tchoffo Ngoula, D., Beier, H., Vormwald, M.: "Fatigue crack growth in cruciform welded joints: Influence of residual stresses and of the weld toe geometry". Fatigue Assessment of Welded Joints by Modern Concepts. Int. J. Fatigue **101**(101), 253–262 (2017). https://doi.org/10.1016/j.ijfatigue.2016.09.020
4. Scuracchio, B.G., de Lima, N.B., Schn, C.G.: Role of residual stresses induced by double peening on fatigue durability of automotive leaf springs. Mater. Des. **47**, 672–676 (2013). https://doi.org/10.1016/j.matdes.2012.12.066
5. Bauschinger, J.: Changes of the elastic limit and the modulus of elasticity on various metals. Zivilingenieur **27**, 289–348 (1881)
6. Cao, J., Lee, W., Cheng, H.S., Seniw, M., Wang, H.-P., Chung, K.: Experimental and numerical investigation of combined isotropic-kinematic hardening behavior of sheet metals. Int. J. Plast **25**(5), 942–972 (2009). https://doi.org/10.1016/j.ijplas.2008.04.007
7. Skrzat, A., Wjcik, M.: An identification of the material hardening parameters for cyclic loading experimental and numerical studies. Arch. Metall. Mater. **65**(2), 779–786 (2020). https://doi.org/10.24425/amm.2020.132820
8. Bruschi, S., Altan, T., Banabic, D., Bariani, P., Brosius, A., Cao, J., Ghiotti, A., Khraisheh, M., Merklein, M., Tekkaya, A.: Testing and modelling of material behaviour and formability in sheet metal forming. CIRP Ann. **63**(2), 727–749 (2014). https://doi.org/10.1016/j.cirp.2014.05.005
9. Rosenschon, M., Merklein, M.: "Process-oriented validation of hardening models in a cyclic bending test". In: Procedia Engineering 207 (2017). International Conference on the Technology of Plasticity, ICTP 2017, 17-22 September 2017, Cambridge, United Kingdom, pp. 1904–1909 (2017) https://doi.org/10.1016/j.proeng.2017.10.959.http://www.sciencedirect.com/science/article/pii/S1877705817357521
10. Rosenschon, M., Suttner, S., Merklein, M.: "Validation of Kinematic Hardening Parameters from Different Stress States and Levels of Plastic Strain with the Use of the Cyclic Bending Test". In: Sheet Metal 2015. Vol. 639. Key Engineering Materials. Trans Tech Publications Ltd, Apr. 2015, pp. 385–392 (2015) https://doi.org/10.4028/www.scientific.net/KEM.639.385.
11. Yin, Q., Soyarslan, C., Gner, A., Brosius, A., Tekkaya, A.: A cyclic twin bridge shear test for the identification of kinematic hardening parameters. Int. J. Mech. Sci. **59**(1), 31–43 (2012). https://doi.org/10.1016/j.ijmecsci.2012.02.008
12. Rosenschon, M., Merklein, M.: "Analysis of the stress and directional dependent Bauschingereffect of sheet metals". In: IOP conference series: materials science and engineering vol. 418, p. 012084 (2018) https://doi.org/10.1088/1757-899x/418/1/012084.https://doi.org/10.1088%2F1757-899x%2F418%2F1%2F012084

13. Steinmann, P.: "Geometrical foundations of continuum mechanics". In: Lecture Notes in Applied Mathematics and Mechanics 2 (2015)
14. Tekkaya, A. E.: A guide for validation of FE-simulations in bulk metal forming. Tech. rep. (2005)
15. Landkammer, P., Jobst, A., Kiener, C., Steinmann, P., Merklein, M.: Investigations on residual stress generation in full-forward-extrusion. Prod. Eng. Res. Devel. **13**(2), 169–180 (2019)
16. Chaboche, J.: Constitutive equations for cyclic plasticity and cyclic viscoplasticity. Int. J. Plast **5**(3), 247–302 (1989). https://doi.org/10.1016/0749-6419(89)90015-6
17. Rudkins, N., Modlen, G., Webster, P.: Residual stresses in cold extrusion and cold drawing: a finite element and neutron diffraction study. J. Mater. Process. Technol. **45**(1), 287–292 (1994). https://doi.org/10.1016/0924-0136(94)90354-9
18. Schwab, W.: Effect of Process Parameters in Metalforming on Fatigue Behaviour. Tech. rep. (1985). https://doi.org/10.1016/S0007-8506(07)61759-4
19. Kannan, S., Srinivasan, S.M.: Influence of manufacturing processes and their sequence of execution on fatigue life of axle house tubes in automobiles. Eng. Fail. Anal. **34**, 79–92 (2013). https://doi.org/10.1016/j.engfailanal.2013.07.013
20. Kergaßner, A., Mergheim, J., Steinmann, P.: Modeling of additively manufactured materials using gradient-enhanced crystal plasticity. Comput. Math. Appl. **356**, 355–356 (2018). https://doi.org/10.1016/j.camwa.2018.05.016
21. Portier, L., Calloch, S., Marquis, D., Geyer, P.: Ratchetting under tensiontorsion loadings: experiments and modelling. Int. J. Plast **16**(3), 303–335 (2000). https://doi.org/10.1016/S0749-6419(99)00056-X
22. DIN 50106:2016-11 Testing of Metallic Materials – Compression Test at Room Temperature. (2016)
23. MSC MARC User Guide. Version (2017)
24. D'Errico, J.: fminsearchbnd, fminsearchcon. MATLAB Central File Exchange. Retrieved February 10, (2020). https://www.mathworks.com/matlabcentral/fileexchange/8277-fminsearchbndfminsearchcon
25. DIN EN ISO 14577:2015-11 Metallic materials Instrumented indentation test for hardness and materials parameters. (2015)
26. Genzel, C., Reimers, W., Malek, R., Phlandt, K.: Neutron and X-ray residual stress analysis of steel parts produced by cold forward extrusion and tube drawing. Mater. Sci. Eng., A **205**(1), 79–90 (1996). https://doi.org/10.1016/0921-5093(95)10005-9
27. Ruud, C. O.: "Residual Stress Measurements". In: Mechanical Testing and Evaluation. ASM International, Jan. (2000). https://doi.org/10.31399/asm.hb.v08.a0003329
28. James, M., Cohen, J.: "1 - The Measurement of Residual Stresses by X-Ray Diffraction Techniques". In: Experimental Methods. Ed. by H. HERMAN. Vol. 19. Treatise on Materials Science & Technology. Elsevier, pp. 1–62 (1980) https://doi.org/10.1016/B978-0-12-341819-7.50007-9.http://www.sciencedirect.com/science/article/pii/B9780123418197500079
29. DIN EN 15305:2009-1 Non-destructive testing – Test method for residual stress analysis by X-ray diffraction (2008)
30. Tekkaya, A. E.: Ermittlung von Eigenspannungen in der Kaltmassivumformung. Springer, Berlin (1986) https://doi.org/10.1007/978-3-642-82799-0
31. Jobst, A., Kiener, C., Merklein, M.: Investigations on residual stress generation in extruded steel components. In: Wulfsberg, J.P., Hintze, W., Behrens, B.-A. (eds.) Production at the Leading Edge of Technology, pp. 83–92. Springer, Berlin (2019)
32. Zucko, M., Phlandt, K., Pyzalla, A., Reimers, W., Kockelmann, H.: Berechnung der Umformeigenspannungen beim Fliepressen und Vergleich mit experimentellen Ergebnissen. Materialwiss. Werkstofftech. **28**(9), 417–423 (1997). https://doi.org/10.1002/mawe.19970280907
33. Hinkfoth, R: "Bulk forming processes". In: Verlagshaus Mainz GmbH, Aachen (2003)
34. Gurtin, M.E., Anand, L., Lele, S.P.: Gradient single-crystal plasticity with free energy dependent on dislocation densities. J. Mech. Phys. Solids **55**(9), 1853–1878 (2007). https://doi.org/10.1016/j.jmps.2007.02.006
35. Miehe, C., Mauthe, S., Hildebrand, F.: Variational gradient plasticity at finite strains. Part III: Localglobal updates and regularization techniques in multiplicative plasticity for single crystals. Comput. Methods Appl. Mech. Eng. **268**, 735–762 (2014). https://doi.org/10.1016/j.cma.2013.08.022
36. Gurtin, M.E.: A theory of grain boundaries that accounts automatically for grain misorientation and grain-boundary orientation. J. Mech. Phys. Solids **56**(2), 640–662 (2008). https://doi.org/10.1016/j.jmps.2007.05.002
37. Arndt, D., Bangerth, W., Blais, B., Clevenger, T.C., Fehling, M., Grayver, A.V., Heister, T., Heltai, L., Kronbichler, M., Maier, M., Munch, P., Pelteret, J.-P., Rastak, R., Thomas, I., Turcksin, B., Wang, Z., Wells, D.: The deal.II Library, Version 9.2. J. Numer. Math. **28**(3), 131–146 (2020). https://doi.org/10.1515/jnma-2020-0043